GDCh Research Article Angewandte International Edition Chemie www.angewandte.org

How to cite: *Angew. Chem. Int. Ed.* **2025**, e22131
doi.org/10.1002/anie.202522131

Batteries

Boosting Magnesium Storage Performance of π-Conjugated Polyimide Cathodes Through Synergistic Molecular and Electrolyte Engineering

Xiaoqian He, Xinyu Sun, Ruiqi Cheng, Lin Hong, Xiaodong Lin, Jie Li, Petru Apostol, Xinlong Xie, Longfei Shao, Viliam Frano, Alexandru Vlad,* and Jianxin Zou**

Abstract: Magnesium metal batteries (MMBs) offer the promise of low cost, intrinsic safety, and high volumetric energy density, but their development is hindered by the scarcity of cathodes capable of reversible Mg^{2+} storage and by cathode–electrolyte incompatibilities. Here, we demonstrate that coupling molecularly engineered polyimide (PI) cathodes with tailored electrolyte speciation enables fast and durable Mg storage. Two PIs, poly(naphthalene tetracarboxylic dianhydride-urea imide) (NUPI) and poly(perylene tetracarboxylic dianhydride-urea imide) (PUPI), with analogous backbones but distinct degrees of π-conjugation were systematically evaluated in both chloride-containing and chloride-free electrolytes. Systematic studies indicate that chloride-free electrolytes, characterized by weakly coordinating anions, enable reversible enolization (C═O ⇌ C─O^-/[C─O^-]$_2Mg^{2+}$) while suppressing side reactions. Additionally, NUPI, featuring stronger π─π stacking and more ordered layered structures, facilitates Mg^{2+} transport and interfacial charge transfer. When combined with a graphene oxide-modified separator, the NUPI cathode delivers 175 mAh g^{-1} at 50 mA g^{-1} and exhibits ultralow capacity fading (≈0.05% per cycle over 1000 cycles at 500 mA g^{-1}). Operando/ex situ spectroscopy analyses and theoretical calculations further confirm the enolization-dominated redox mechanism. This work establishes a molecular-electrolyte co-design paradigm for high-rate, durable MMBs based on carbonyl polymer chemistry.

Introduction

The accelerating transition to renewable electricity and electrified transport demands rechargeable batteries that surpass the energy, cost, and safety profiles of conventional lithium-ion technology.[1–3] Among post-lithium chemistries, magnesium metal batteries (MMBs) are attractive owing to magnesium's natural abundance, low cost, non-dendritic plating propensity, and high theoretical volumetric capacity (3832 mAh cm^{-3}).[4] Yet, practical MMBs remain nascent. The central bottleneck is the cathode: few materials can reversibly host Mg^{2+} with high capacity, high rate capability, and long cycle life. These difficulties stem from the small ionic radius (≈0.72 Å) and high charge density of Mg^{2+}, which engender strong Coulombic interactions with host material lattices and solvents, slow desolvation/diffusion, large overpotentials, and pervasive incompatibilities with common electrolytes and cathode frameworks.

Organic cathodes have emerged as compelling alternatives due to the chemical tunability, mechanical compliance, and potential sustainability of their redox-active motifs and molecular backbones.[5,6] Among them, carbonyl-based compounds demonstrate strong potential for Mg storage. During discharge, carbonyl groups are electrochemically reduced to enolate structures, whose oxygen atoms coordinate with Mg^{2+} ions from the electrolyte. Upon charging, the original carbonyl functionality is readily and reversibly restored, offering a level of redox reversibility rarely achieved in conventional inorganic cathode systems.[7] However, small-molecule carbonyls tend to dissolve, compromising cyclability.

[*] X. He, X. Sun, X. Xie, L. Shao, J. Zou
National Engineering Research Center of Light Alloys Net Forming and State Key Laboratory of Metal Matrix Composites, Center of Hydrogen Science, School of Materials Science and Engineering, Shanghai Jiao Tong University, Shanghai 200240, P.R. China
E-mail: zoujx@sjtu.edu.cn

X. He, X. Lin, P. Apostol, V. Frano, A. Vlad
Institute of Condensed Matter and Nanosciences, Molecular Chemistry, Materials and Catalysis, Université catholique de Louvain, Louvain-la-Neuve B-1348, Belgium
E-mail: xiaodong.lin@uclouvain.be
alexandru.vlad@uclouvain.be

R. Cheng
Department of Applied Biology and Chemical Technology, The Hong Kong Polytechnic University, Hong Kong 999077, P.R. China

L. Hong
School of Mechanical Engineering, National Engineering Laboratory of Automobile Electronics and Control Technology, Shanghai Jiao Tong University, 800 Dongchuan Road, Shanghai 200240, P.R. China

J. Li
School of Chemistry and Chemical Engineering, Shanghai Jiao Tong University, Shanghai 200240, P.R. China

A. Vlad
WEL Research Institute, avenue Pasteur, 6, Wavre 1300, Belgium

Additional supporting information can be found online in the Supporting Information section

Converting these motifs into polymers mitigates dissolution and improves structural integrity. Polyimides (PIs), built from imide units bearing two carbonyls bridged by nitrogen, exhibit rigid, planar backbones that promote crystallinity as well as thermal/mechanical robustness.[8,9] Their terminal carbonyls can, in principle, support multi-electron redox with theoretical capacities exceeding 100 mAh g^{-1}. In practice, however, reported PI cathodes often suffer from limited electronic conductivity, sluggish ion transport, and aggregation of polymer chains, leading to partial utilization of redox sites and modest rate performance.

Molecular engineering provides routes to address these intrinsic constraints.[10] Introducing electron-withdrawing groups or flexible linkers can tune the local electronic environment of carbonyls, stabilize intermediates, and buffer structural changes during cycling. Designing π-extended, planar-building blocks strengthens π–π interactions, encourages layered microstructures, and can facilitate through-plane ion/electron transport. Nevertheless, these benefits must be balanced against a key trade-off: greater conjugation typically reduces the density of redox-active carbonyls per mass, potentially lowering theoretical capacity. Therefore, rational PI design requires simultaneous optimization of redox site density, electronic delocalization, and mesoscale ordering.

Electrolyte chemistry is equally decisive. The identity and speciation of Mg salts and solvents dictate Mg^{2+} solvation structures, desolvation barriers, interfacial charge transfer, and oxidative stability.[11,12] Nucleophilic electrolytes can attack electrophilic carbonyls, driving parasitic reactions; by contrast, non-nucleophilic systems, with weakly coordinating anions or sterically hindered frameworks, suppress such degradation.[13] Representative systems include magnesium monocarborane [$Mg(CB_{11}H_{12})_2$], magnesium aluminum chloride complex (MACC), magnesium tetrakis(hexafluoroisopropyloxy)borate [$Mg[B(hfip)_4]_2$, hfip = $OCH(CF_3)_2$], and magnesium bis(hexamethyldisilazide) [$Mg(HMDS)_2$, HMDS = $N(Si(CH_3)_3)_2$] often incorporating Lewis acids such as $AlCl_3$, $MgCl_2$, etc. A critical distinction across these systems is the presence of chloride. Chloride can remove passivation on Mg metal and facilitate plating/stripping, yet it may also promote corrosion and cathode/electrolyte side reactions; chlorine-free electrolytes generally offer higher oxidative stability and wider voltage windows, but require interphases that permit efficient Mg^{2+} transport.

Despite these advances, a systematic understanding of how PI molecular structure couples with electrolyte chemistry (especially in chloride-containing vs. chloride-free systems) to govern Mg-storage performance remains limited. Addressing this gap is essential for the rational co-design of PI cathodes and electrolytes to realize the full potential of these materials and deliver high-capacity, high-rate, and durable MMBs.

Here, we designed two PIs with similar backbones but distinct π-conjugation, poly(naphthalene tetracarboxylic dianhydride-urea imide) (NUPI) and poly(perylene tetracarboxylic dianhydride-urea imide) (PUPI), and explored their coupling with chloride-containing and chloride-free electrolytes. Our results revealed that chloride-containing electrolytes, owing to their narrower electrochemical stability windows and more reactive speciation, limit the extent and reversibility of enolization in PI frameworks and thus restrict the accessible capacity. By contrast, the chloride-free electrolyte offers a broader stability voltage window and more benign interfacial chemistry, enabling deeper, more reversible enolization of active sites, and thus delivering higher reversible capacities. Molecular structure further governs performance: relative to PUPI, whose irregular microstructure exhibits weaker π–π stacking, NUPI forms uniform, layered structure with stronger π–π interactions that facilitate interlayer charge transport and Mg^{2+} insertion/deinsertion, yielding superior Mg storage capacity. Leveraging these insights, by combining NUPI with chloride-free electrolyte and a graphene-oxide-modified separator to suppress shuttling of soluble intermediates, the corresponding MMBs deliver ≈175 mAh g^{-1} at 50 mA g^{-1} and sustain an ultralow discharge-capacity decay of ≈0.05% per cycle over 1000 cycles at 500 mA g^{-1}. Ex situ/in situ characterizations and density functional theory (DFT) calculations uncover a heterogeneous enolization redox pathway (C═O ↔ C─O^-) as the basis for fast, reversible Mg storage. Collectively, these findings elucidate the interplay between PI molecular structure and electrolyte chemistry in governing Mg^{2+} transport and interfacial stability, and establish a broadly applicable co-design strategy for high-performance MMBs.

Results and Discussion

The two PIs, NUPI and PUPI, studied in this work were synthesized via polycondensation of the corresponding aromatic dianhydrides, 1,4,5,8-naphthalenetetracarboxylic dianhydride (NTCDA) and 3,4,9,10-perylenetetracarboxylic dianhydride (PTCDA), with diamine precursors under reflux in N_2, followed by high-temperature annealing to complete imidization (Figure S1). Both polymers consist of imide units (─CO─N─CO─) along rigid, π-conjugated backbones, with theoretical capacities of 183 mAh g^{-1} for NUPI and 123 mAh g^{-1} for PUPI, respectively. Although non-conjugated carbonyl groups are generally considered electrochemically inactive, they can provide additional rotational flexibility and enhance coordination or stabilization effects. DFT-derived electrostatic potential (ESP) maps (Figure 1a) resolve likely reactive/coordination sites: negative ESP (red) localizes at carbonyl oxygens, identifying nucleophilic, electron-rich centers capable of coordinating Mg^{2+}, whereas positive ESP (blue) marks electron-deficient domains across the extended aromatic rings. Fourier transform infrared (FTIR) spectra confirm successful imidization (Figure 1b): the anhydride vibrations of NTCDA/PTCDA (C─O─C and ─CO─O─CO─) disappear, while strong imide C═O asymmetric/symmetric stretches emerge (NUPI: 1740–1680 cm^{-1}; PUPI: 1720–1670 cm^{-1}). Additional bands near 1780 cm^{-1} (NUPI) and 1760 cm^{-1} (PUPI) are assigned to urea-derived carbonyls; bands around 1580 cm^{-1} correspond to aromatic C═C stretching, and C─N stretching at ~1346 cm^{-1} (NUPI) and ~1360 cm^{-1} (PUPI) is characteristic of the imide ring. Relative to the monomers, modest red shifts of the carbonyl

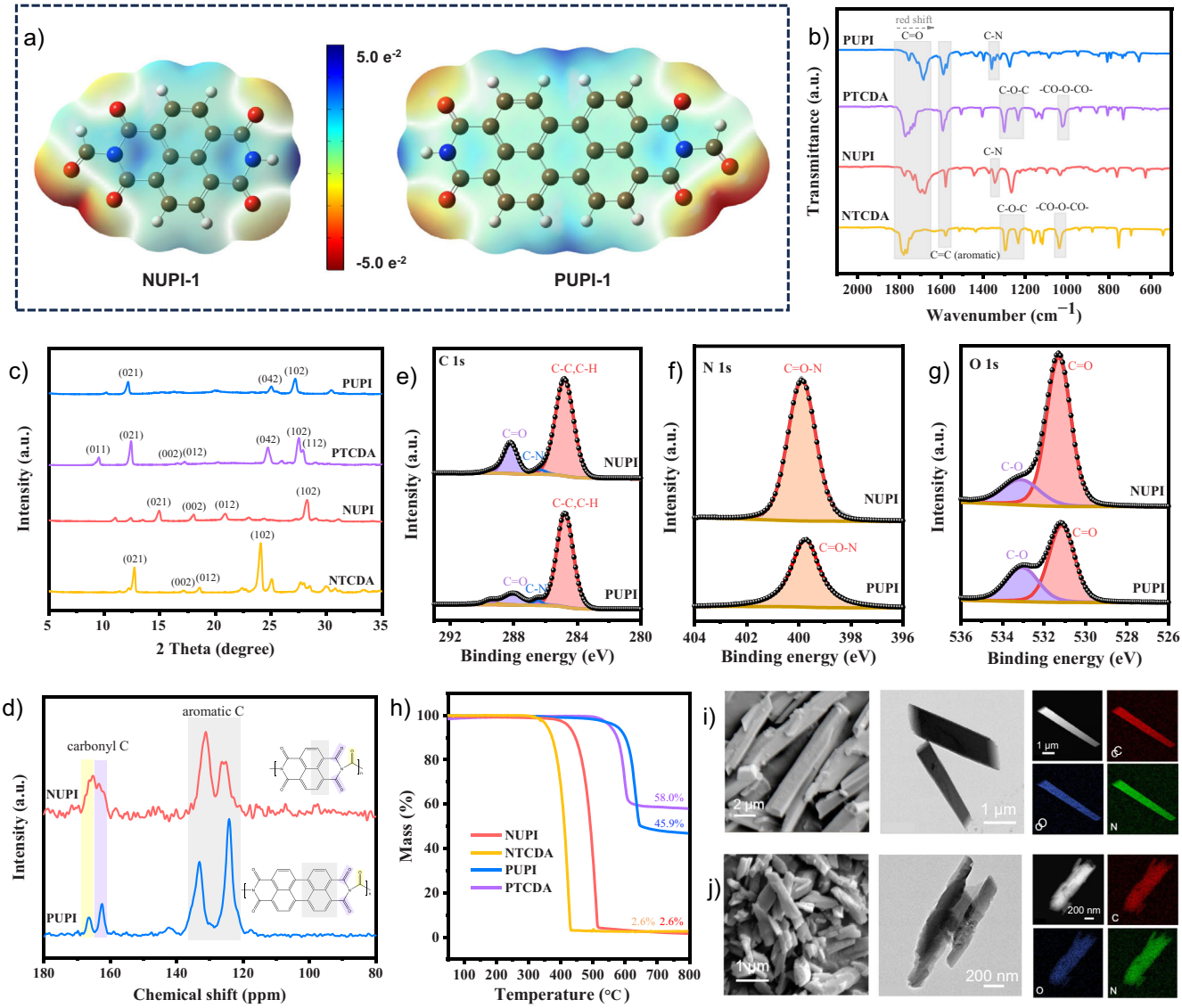

Figure 1. Structure and characterization of polyimides NUPI and PUPI. a) DFT calculated ESP maps. b) FTIR spectra. c) Powder XRD patterns. d) Solid-state ^{13}C NMR spectra. (e–g) High-resolution XPS C 1s, N 1s, and O 1s spectra. h) Thermogravimetric analysis curves. i) and j) SEM, TEM, HAADF-STEM images, and EDS elemental maps for (i) NUPI and (j) PUPI, respectively.

bands in both PIs are consistent with increased conjugation upon imidization.[14]

Powder X-ray diffraction (XRD) demonstrates pronounced crystallinity in both polymers and clear divergence from their monomers (Figure 1c). Diffraction peaks characteristic of NTCDA and PTCDA are absent in the polymer patterns, consistent with complete monomer consumption and successful polycondensation. For NUPI, several reflections appear at higher 2θ than in NTCDA, indicating reduced d-spacings and tighter packing; this trend is consistent with increased conjugation and densification upon diamine incorporation and imidization. A prominent diffraction peak at $2\theta \approx 28.2°$ is attributed to strong interlayer π–π stacking, which can facilitate through-stack charge transport via close-packed alignment of delocalized π-systems.[15] Because the conjugated PIs are poorly soluble in standard deuterated solvents, solid-state ^{13}C NMR was used for structural assignment (Figure 1d). The most downfield resonance at ~166 ppm is attributed to the urea carbonyl carbons, consistent with bonding to electronegative nitrogen and the lack of conjugation with the PI π-system. A distinct signal at ~163 ppm corresponds to imide carbonyls derived from the dianhydride units within the PI rings. Additional resonances between 120 and 140 ppm arise from aromatic backbone carbons. Collectively, these well-resolved features indicate a high degree of structural order and corroborate the successful synthesis of extended π-conjugated PIs.[16]

X-ray photoelectron spectroscopy (XPS) was used to further probe the polymer composition. The survey spectra display the expected C 1s, N 1s, and O 1s signals at ~284, 400, and 531 eV, respectively (Figure S2).[17] High-resolution spectra (Figure 1e–g) resolve C 1s components at ~284.8 eV (C─C/C─H), ~286.0 eV (C─N), and ~288.0 eV (C═O); an N 1s contribution centered at ~398.8 eV assigned to the

imide C═O─N moiety; and O 1s features at ~531.4 eV (imide C═O) and ~533.5 eV (C─O species, possibly from processing intermediates or residuals). Compared with the corresponding dianhydrides (Figure S3), the enhanced carbonyl contribution in the polymer spectra corroborates successful polycondensation with urea. Thermogravimetric analysis indicates high thermal stability after polymerization (Figure 1h).

Scanning electron microscopy (SEM) and transmission electron microscopy (TEM) reveal distinct morphologies for the two PIs (Figures 1i,j). NUPI forms uniform, layer-stacked, rod-like particles with a well-ordered lamellar texture and larger characteristic dimensions, consistent with stronger π–π interactions and higher crystallinity. By contrast, PUPI appears as irregular, bar-like fragments with less pronounced layering.[18] High-angle annular dark-field scanning transmission electron microscopy (HAADF-STEM) and energy-dispersive X-ray spectroscopy (EDS) mapping show homogeneous distributions of C, N, and O across both samples. Consistent with its compact and uniform lamellae, NUPI exhibits lower specific surface area and pore volume than PUPI in N_2 adsorption–desorption measurements (Figure S4), indicative of tighter interlayer stacking.

Before investigating the coupling interactions between the two PI molecules and different electrolytes, we first conducted benchmark tests on two non-nucleophilic electrolytes: a chlorine-free $Mg[B(hfip)_4]_2$/1,2-dimethoxyethane (DME) and a chlorine-containing $Mg(HMDS)_2$-$MgCl_2$-$AlCl_3$/tetraethylene glycol dimethyl ether (TEGDME) system. The successful synthesis of the $Mg[B(hfip)_4]_2$ salt is confirmed by the characterization results shown in Figures S5 and S6. Cyclic voltammetry (CV) on stainless-steel (SS) foil at 5 mV s^{-1} between −1 and 3 V was used to evaluate Mg plating/stripping behavior (Figure 2a,d). In the $Mg(HMDS)_2$-based electrolyte, the cathodic current associated with Mg plating appears at −0.27 V, whereas anodic stripping initiates at 0.16 V and increases sharply to a peak near 0.82 V (Figure 2a). In contrast, the $Mg[B(hfip)_4]_2$-based electrolyte exhibits a plating onset at −0.20 V and a stripping onset at 0.28 V, with a similar anodic peak at ~0.82 V (Figure 2d). Although both electrolytes support reversible Mg deposition/stripping and yield comparable peak currents over subsequent cycles, $Mg[B(hfip)_4]_2$/DME delivers a higher deposition current density and greater electrochemical stability upon cycling.

To assess oxidative stability, linear sweep voltammetry (LSV) was performed on Al, Mo, Cu, and SS current collectors at scan rates of 0.5 and 5 mV s^{-1} (Figures 2b,e and S7). Across scan rates, both electrolytes show consistent trends: the chlorine-free $Mg[B(hfip)_4]_2$/DME sustains oxidation ≥3.0 V versus Mg^{2+}/Mg on all current collectors, indicating a wider oxidative window than the chloride-containing $Mg(HMDS)_2$-$MgCl_2$-$AlCl_3$/TEGDME (Figure 2b,e). In particular, on Al, the $Mg(HMDS)_2$-based electrolyte is oxidatively unstable below ~2.0 V, attributable to chloride-induced corrosion. Mg||Mg symmetric cells further elucidate the trade-off between the two electrolyte systems (Figure 2c,f). At 0.1 mA cm^{-2}, both electrolytes undergo an interfacial activation phase characterized by a gradual decrease in polarization during the initial cycles; after ~400 h, the chloride-containing electrolyte exhibits lower voltage hysteresis (Figure 2c). However, at higher current density (0.5 mA cm^{-2}), the chlorine-free $Mg[B(hfip)_4]_2$/DME maintains lower overpotentials (Figure 2f), consistent with a more stable solid-electrolyte interphase (SEI) that enables efficient Mg^{2+} transport under demanding conditions. Collectively, these observations indicate that chloride-containing electrolytes facilitate interfacial activation at low current densities but their corrosivity and side reactions can compromise stability at elevated rates,[19] whereas the chlorine-free system forms a favorable SEI on Mg surface and preserves high-voltage tolerance across substrates.[20]

We also investigated the Mg plating/stripping behavior of the two studied electrolyte systems in Mg||Mo half-cells. Long-term cycling at 0.1 mA cm^{-2} with an upper cutoff voltage of 1.0 V is shown for the chlorine-free $Mg[B(hfip)_4]_2$/DME and the chloride-containing $Mg(HMDS)_2$-$MgCl_2$-$AlCl_3$/TEGDME in Figure 2g,j, respectively, with the corresponding Coulombic efficiency and polarization evolution summarized in Figure 2h,k. In $Mg[B(hfip)_4]_2$, Coulombic efficiencies of 89.6%, 91.4%, 91.4%, and 93.0% are obtained at the 20th, 50th, 100th, and 200th cycles with polarizations of 0.20, 0.19, 0.20, and 0.25 V, respectively (Figure 2h). In the $Mg(HMDS)_2$-based electrolyte, the corresponding values are 87.6%, 91.1%, 93.4%, and 94.3% with polarizations of 0.22, 0.20, 0.19, and 0.18 V (Figure 2k). Rate capability tests on Mg||Mo cell (Figure 2i,l) focus on plating/stripping overpotentials and, together with LSV on Mo, enable comparison of oxidation stability on this current collector. The chloride-containing electrolyte exhibits lower overpotential during the initial cycles, indicating faster interfacial kinetics (Figure 2i,l),[21] whereas $Mg[B(hfip)_4]_2$ requires interphase formation—SEI on the Mg surface and, upon oxidation, cathode–electrolyte interphase at the cathode/electrolyte interface—which temporarily penalizes early-cycle performance.[22] Nevertheless, the higher accessible cutoff voltages on Mo in $Mg[B(hfip)_4]_2$ (Figure S8) underscore its broader oxidative window and potential compatibility with higher-voltage cathodes. These behaviors are consistent with the Mg||Mg symmetric-cell results: chloride helps disrupt or destabilize insulating passivation and facilitates Mg^{2+} transport at low current densities but limits the usable voltage range, while the chlorine-free electrolyte supports a more stable interphase and higher-voltage operation.

Speciation analysis (Equations (4–7) in the Experimental Procedures section of the Supporting Information) reveals that the chloride-containing $Mg(HMDS)_2$-$MgCl_2$-$AlCl_3$/TEGDME electrolyte comprises a complex mixture of monovalent species (e.g., $Mg_2Cl_3^+$, $HMDSAlCl_3^-$, $MgCl^+$, $AlCl_2^+$, $AlCl_4^-$), whereas the chlorine-free $Mg[B(hfip)_4]_2$/DME predominately features divalent Mg^{2+} cations paired with weakly coordinating $[B(hfip)_4]^-$ anions. To probe how speciation impacts electrode behavior, we systematically recorded cyclic voltammograms of NUPI and PUPI in both electrolytes under different voltage windows (Figure 3a). In the chloride-containing electrolyte, reactive monovalent complexes are likely to interact with

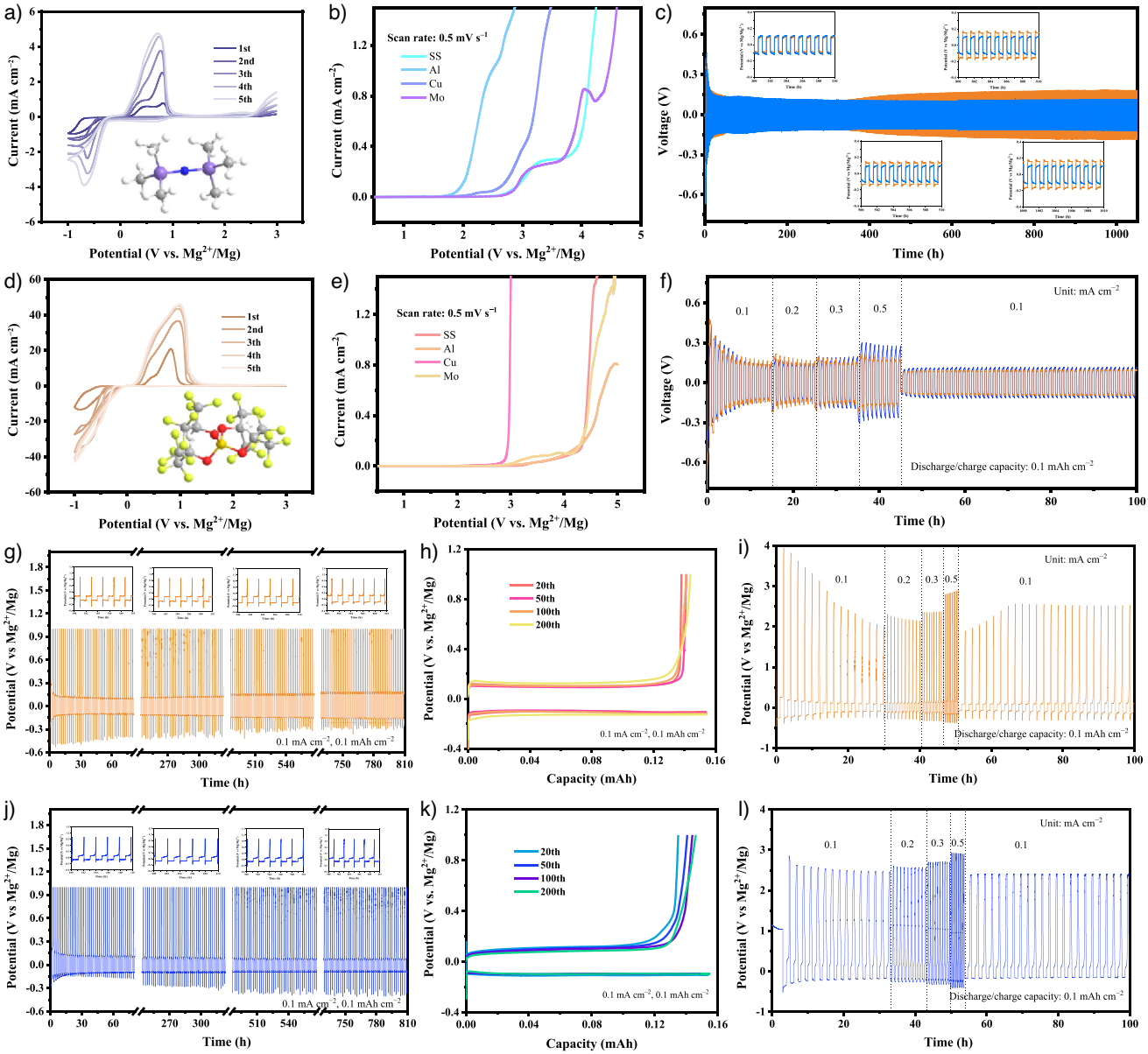

Figure 2. Electrochemical benchmarking of chlorine-containing and chlorine-free electrolytes. a) and d) CVs of Mg||SS half-cells with (a) $Mg(HMDS)_2$-$MgCl_2$-$AlCl_3$/TEGDME and (d) $Mg[B(hfip)_4]_2$/DME at 5 mV s^{-1}. b) and e) LSVs on Al, Mo, SS, and Cu working electrodes in (b) $Mg(HMDS)_2$-$MgCl_2$-AlCl3/TEGDME and (e) $Mg[B(hfip)_4]_2$/DME at 0.5 mV s^{-1}. c) and f) Galvanostatic Mg plating/stripping of Mg||Mg symmetric cells in $Mg(HMDS)_2$-$MgCl_2$-$AlCl_3$/TEGDME (blue) and $Mg[B(hfip)_4]_2$/DME (orange) at (c) 0.1 mA cm^{-2} and (f) various current densities ranging from 0.1 to 0.5 mA cm^{-2}, with an areal capacity of 0.1 mAh cm^{-2}. g) and j) Long-term cycling of Mg||Mo half-cells in (g) $Mg[B(hfip)_4]_2$/DME and (j) $Mg(HMDS)_2$-$MgCl_2$-$AlCl_3$/TEGDME at 0.1 mA cm^{-2} (upper cutoff 1.0 V). h) and k) Voltage profiles of the Mg||Mo half-cells in (h) $Mg[B(hfip)_4]_2$/DME and (k) $Mg(HMDS)_2$-$MgCl_2$-$AlCl_3$/TEGDME at the 20th, 50th, 100th, and 200th cycles. i) and l) Galvanostatic plating/stripping curves of Mg||Mo half-cells in (i) $Mg[B(hfip)_4]_2$/DME and (l) $Mg(HMDS)_2$-$MgCl_2$-$AlCl_3$/TEGDME at varied current densities.

the conjugated backbones, disrupting crystallinity and suppressing reversible redox processes, particularly during deep discharge to 0.01 V (Figure 3a(II,IV)). By contrast, in chlorine-free $Mg[B(hfip)_4]_2$-based system, both PIs display well-defined, reversible peaks even at a 0.01 V cutoff, with higher current densities than at a 0.7 V cutoff (Figure 3a(I,III)). Accordingly, robust redox is observed over 0.01–2.5 V (vs. Mg^{2+}/Mg) in $Mg[B(hfip)_4]_2$ and over 0.7–2.4 V in the $Mg(HMDS)_2$-based electrolyte. Although both PIs exhibit reduction at higher potentials in the chloride-containing electrolyte, the corresponding oxidation peaks are largely absent, indicating poor reversibility (Figure S9). This behavior may be attributed to the anodic sweep being truncated by the limited upper cutoff potential imposed by the electrolyte's low oxidative stability. Consistently, NUPI and PUPI deliver extremely low capacity with fading plateaus in the chloride-containing system (Figure S9), whereas in $Mg[B(hfip)_4]_2$/DME electrolyte, both PIs achieve higher capacities (Figures S10 and S11), benefiting from a favorable discharge cutoff voltage of 0.01 V.

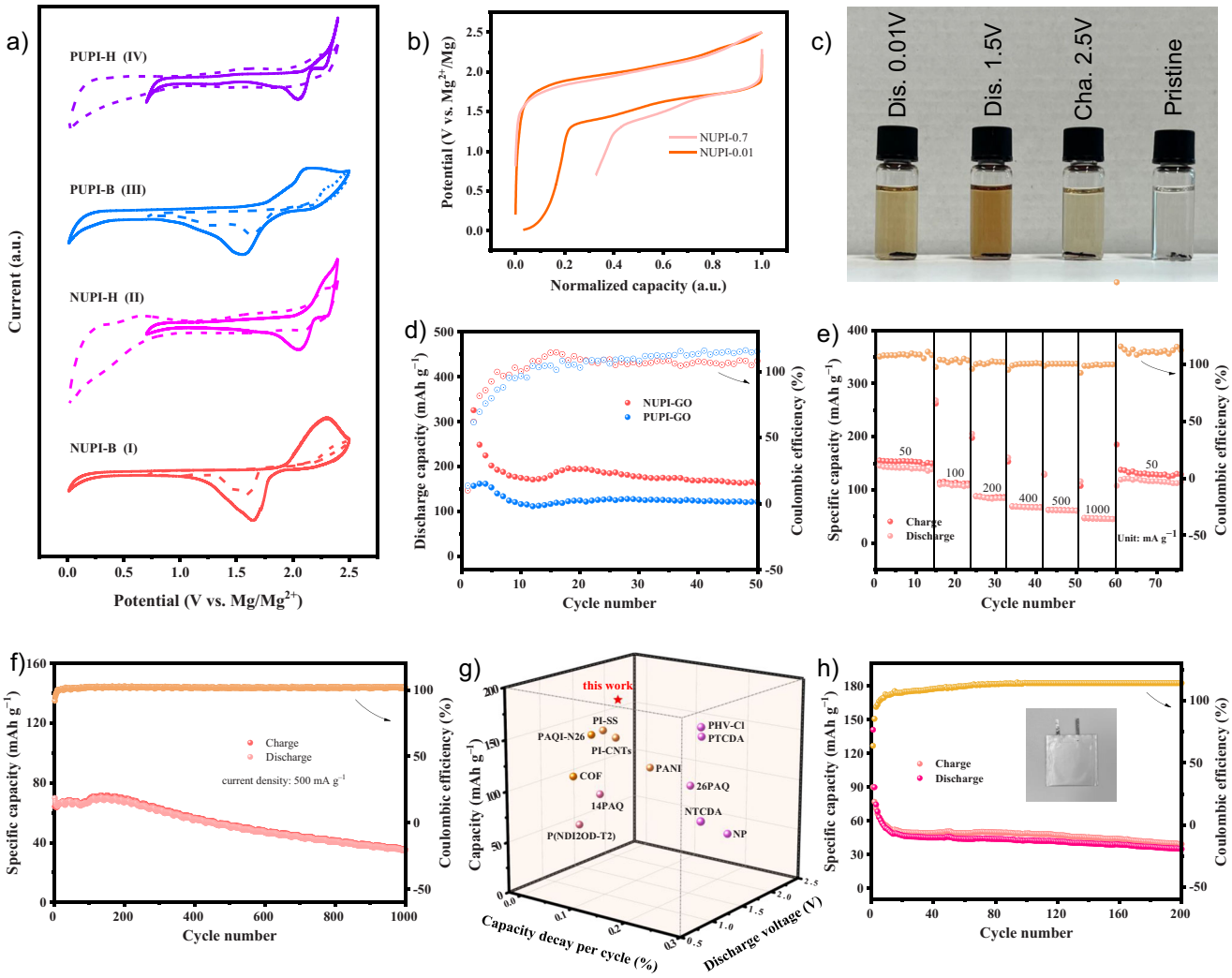

Figure 3. Electrochemical behavior of NUPI and PUPI in chlorine-free and chloride-containing electrolytes. a) CVs of NUPI and PUPI at 0.1 mV s^{-1} over different voltage windows in (II, IV) $Mg[B(hfip)_4]_2$- and (I, III) $Mg(HMDS)_2$-based electrolytes. b) Galvanostatic charge–discharge curves of NUPI from 0.01–2.5 V and 0.7–2.5 V in $Mg[B(hfip)_4]_2$ at 100 mA g^{-1}. c) Optical photographs of NUPI electrodes at selected states after immersion in DME for 30 min. d) Cycling performance of NUPI and PUPI with GO-modified separators in $Mg[B(hfip)_4]_2$-based electrolyte at 50 mA g^{-1}. The Coulombic efficiency exceeding 100% is likely due to a mild shuttle effect caused by incomplete suppression of soluble intermediates by the GO membrane. e) and f) Rate capability at various current densities ranging from 50 to 1000 mA g^{-1}, corresponding to 0.27–5.46 C (1 C = 183 mA g^{-1}). (e) and long-term cycling stability at 500 mA g^{-1} (f) of NUPI-based cells with a GO-modified separator in $Mg[B(hfip)_4]_2$-based electrolyte system. g) Benchmark of this work against recently reported cathodes. h) Cycling stability of a pouch-type NUPI||Mg cell in the $Mg[B(hfip)4]2$-based electrolyte at 50 mA g−1 without GO-modified separator (inset: photograph of the pouch cell).

Normalized capacity-voltage profiles of NUPI||Mg cells with the chlorine-free $Mg[B(hfip)_4]_2$/DME electrolyte (Figure 3b) enable a direct comparison between discharge cutoff voltages of 0.01 and 0.7 V. Notably, the 0.01 V protocol (NUPI-0.01) delivers a higher discharge capacity and a slightly lower overpotential than 0.7 V (NUPI-0.7), highlighting the electrode's electrochemical stability and broad voltage tolerance in this electrolyte—an outcome that contrasts the common behavior of organic cathodes, where deeper discharge typically accelerates degradation and worsens cycling.[23] To further elucidate the underlying mechanism, the dissolution behavior of NUPI electrodes before and after cycling was investigated. Figures 3c and S12 present optical images of NUPI electrodes immersed in DME for 30 min. The pristine electrode remains insoluble, yielding a colorless solution, while all cycled electrodes display varying degrees of brown coloration. Discharge to 1.5 V produces a dark brown solution, whereas further discharge to 0.01 V reduces the color intensity, indicating lower solubility of the fully discharged product. Upon charging to 2.5 V, the solution becomes lighter, suggesting partial recovery of the pristine state. Such phenomena have been previously described as heterogeneous liquid–solid reactions,[24] further supporting 0.01 V as a more favorable discharge cutoff voltage. The structural evolution of the electrode is proposed to rationalize this dissolution behavior during cycling. Initial Mg^{2+} insertion disrupts π–π stacking among PI chains, leading to amorphization and increased solubility. As Mg^{2+}

uptake progresses, the formation of strong intermolecular O···Mg···O coordination bonds enhances structural integrity, reducing solubility, and facilitating redeposition of active material.[25]

Given the liquid–solid reaction pathway and the presence of soluble intermediates that can leach active material and passivate the Mg anode, we cast a graphene-oxide (GO) coating onto glass-fiber separators to hinder shuttle while maintaining Mg^{2+} transport.[24] The carbonyl groups in GO undergo an irreversible reduction during the first discharge, producing a large initial irreversible capacity; thereafter, the GO film and conductive carbon contribute negligibly to capacity (Figure S13). Furthermore, XPS analysis (Figure S14) shows that GO undergoes partial reduction to rGO during the initial cycles, evidenced by decreased oxygen functionalities, thereby serving primarily as a physical barrier. With GO-modified separators in the chlorine-free $Mg[B(hfip)_4]_2$/DME electrolyte—operated within the optimized 0.01–2.5 V window—both PIs deliver very high first-cycle capacities at 50 mA g^{-1} (Figure 3d), primarily due to GO reduction and concomitant interphase formation with the electrolyte, in agreement with prior reports (Figure S15).[26,27] Subsequently, NUPI exhibits higher capacities and more stable cycling than PUPI, attributed to its lower molecular weight per redox unit and more efficient active site utilization enabled by its ordered, layer-stacked structure (Figure S16).[28] Specifically, the PUPI cathode retains a discharge capacity of ~120 mAh g^{-1} after 50 cycles, whereas the NUPI cathode maintains ~160 mAh g^{-1} in the 50th cycle.

Figure 3e presents the rate performance of the NUPI cathode across a range of current densities from 50 to 1000 mA g^{-1}. As expected, the specific capacity decreases with increasing current density but recovers when the current returns to 50 mA g^{-1}. The NUPI cathode delivers high discharge capacities of approximately 160, 110, 90, 75, 70, and 55 mAh g^{-1} at 50, 100, 200, 400, 500, and 1000 mA g^{-1}, respectively (Figure S17). Figure 3f shows the long-term cycling stability of the NUPI cathode coupled with a GO membrane at 500 mA g^{-1}, exhibiting a low capacity decay rate of ~0.05% per cycle over 1000 cycles. Comparison with recent reports (Figure 3g and Tables S1 and S2) underscores the favorable balance of capacity and durability achieved in this work. To evaluate practical applicability, a NUPI-based pouch cell was assembled, exhibiting an open-circuit voltage (OCV) above 1.8 V. When two such cells were connected in series, they successfully powered a 3 V light bulb (Figure S18). The cycling curves and charge/discharge profiles (Figures 3h and S19) further corroborate the excellent electrochemical performance of the NUPI cathode in the chlorine-free $Mg[B(hfip)_4]_2$ electrolyte.

To investigate the diffusion kinetics of both cathodes, galvanostatic intermittent titration technique (GITT) measurements were conducted to determine the Mg^{2+} diffusion coefficient (D_{Mg2+}). As shown in Figure 4a,b, the D_{Mg2+} values for NUPI are consistently higher than those for PUPI throughout the cycling process, indicating enhanced Mg^{2+} diffusion in the layer-stacked, π-conjugated NUPI structure featuring strong π–π interactions.[29] Subsequently, CV measurements were performed on NUPI at various scan rates (Figure 4c). A distinct reduction peak at approximately 1.6 V and an oxidation peak near 2.2 V are observed, corresponding well to the discharge/charge plateaus. The peak current densities increase with increasing scan rate. According to Equations (9) and (10) in the Supporting Information, a b-value of 0.5 indicates a diffusion-controlled intercalation process, whereas $b = 1$ suggests a surface-controlled capacitive process. The calculated b-values for NUPI are 0.556 for the reduction peak and 0.649 for the oxidation peak (Figure 4d), indicating a mixed-controlled electrochemical process. Furthermore, Equation (11) was applied to quantitatively distinguish capacitive and diffusion-controlled contributions. As illustrated in Figure 4e, the capacitive contribution accounts for 53% of the total current at a scan rate of 0.5 mV s^{-1}. This proportion increases progressively with scan rate, reaching 89% at 4.0 mV s^{-1} (yellow-shaded area, Figure 4f). These results indicate that Mg^{2+} storage in NUPI is predominantly pseudocapacitive at high current densities, as reflected by the nearly linear charge–discharge profiles lacking distinct voltage plateaus (Figure S17). This behavior arises from surface-accessible redox sites such as edge carbonyls and defect-related regions within moderately disordered π–π stacking domains, which facilitate rapid electron transfer.[30]

To elucidate the Mg^{2+} storage mechanism in conjugated PI cathodes using the $Mg[B(hfip)_4]_2$/DME electrolyte, a combination of ex situ and in situ spectroscopic techniques was employed. Figures 5a and S20a present the ex situ FTIR spectra of NUPI and PUPI electrodes collected at defined states during the 5th cycle under two voltage windows: 0.01–2.5 V and 0.7–2.5 V. The imide C=O stretching band (~1700 cm^{-1}) progressively weakens and eventually disappears upon magnesiation (discharge), while a new band emerges at ~1190 cm^{-1}, corresponding to the $[C{-}O^-]_2Mg^{2+}$ (enolate) stretching vibration. During subsequent de-magnesiation (charging), the C=O band reappears and the $[C{-}O^-]_2Mg^{2+}$ band diminishes. Notably, the $[C{-}O^-]_2Mg^{2+}$ band is significantly more intense in NUPI electrodes discharged to 0.01 V than in those discharged to 0.7 V, suggesting that the wide electrochemical stability window of the $Mg[B(hfip)_4]_2$/DME electrolyte enables more extensive enolization at active sites, thereby unlocking higher capacity. In contrast, electrolytes with narrower voltage windows will inevitably constrain the extent of enolization, limiting capacity output in such organic cathodes. In situ synchrotron FTIR (SR-FTIR) measurements further confirm the reversibility of the enolization-based redox mechanism in NUPI cathodes. As shown in Figure 5b, during discharge, the $[C{-}O^-]_2Mg^{2+}$ band (~1190 cm^{-1}) intensifies, while the intensities of the C=O (1680–1700 cm^{-1}) and C=C (~1580 cm^{-1}) bands decrease—changes that reverse upon charging. These findings not only validate the reversible enolization mechanism in NUPI, but also underscore the crucial role of cathode–electrolyte compatibility in enabling high-performance magnesium-organic batteries.

In situ synchrotron XRD (SR-XRD; Figures 5c and S21) and ex situ XRD (Figure S22) were further used to monitor the structural evolution of NUPI during cycling. Due to the shorter wavelength (λ) of high-energy synchrotron radiation

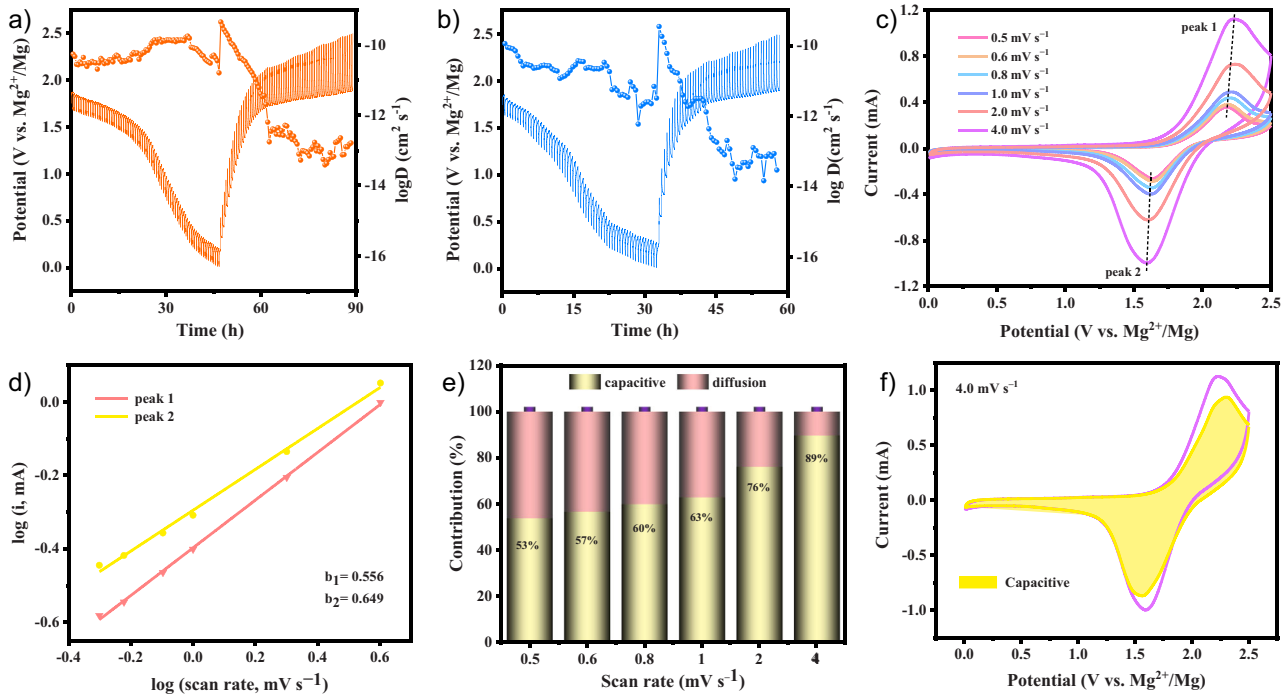

Figure 4. Diffusion kinetics and charge-storage behavior of NUPI and PUPI in $Mg[B(hfip)_4]_2$-based electrolyte. a) and b) GITT profiles and Mg^{2+} diffusion coefficients (D_{Mg2+}) for NUPI and PUPI. c) CVs of NUPI-based cells at scan rates of 0.5–4.0 mV s^{-1}. d) log i∼log ν plots used to extract b values. e) Capacitive-contribution fraction of NUPI-based cells versus scan rate. f) CV profile of the NUPI cathode with the pseudocapacitive contribution at a scan rate of 4.0 mV s^{-1}.

compared to conventional Cu K_α sources, Bragg reflections are shifted to lower 2θ angles, as shown in Figure S21. Distinct diffraction peaks at 8.4°, 9.7°, and 12.0°, indexed to the (002), (012), and (102) planes of the conjugated backbone, attenuate upon discharge and reappear upon charging over two cycles, indicating highly reversible, potential-dependent Mg^{2+} (de)intercalation processes. Notably, the (102) diffraction peak, associated with π–π stacking, shifts to a lower angle during the fifth discharge-charge cycle as compared to the pristine electrode state (Figure S22). This shift indicates a partially irreversible interlayer expansion and structural rearrangement of the NUPI framework following Mg^{2+} insertion/extraction in the early cycles.[29] Interestingly, during the fifth and subsequent cycles (Figures 5c and S22), the NUPI electrode displays only reversible variations in peak intensity, with the (102) peak position remaining unchanged. These results suggest that the overall layered framework stabilizes after the initial structural reorganization. Ex situ XPS further substantiates the enolization-based storage mechanism in NUPI (Figures 5e–g and S23). In the C 1s spectrum—deconvoluted into C─F (originating from $[B(hfip)_4]^-$ anions and the PVDF binder), C═O, C─O/C─N, and C─C/C─H components—the intensity of the C─O signal progressively increases while that of C═O decreases during discharge, consistent with Mg^{2+} insertion into the NUPI backbone. This trend reverses upon charging. It is worth mentioning that the weak C─O signal observed in the pristine electrode can be attributed to surface functional groups on the conductive carbon and/or cathode–electrolyte interphase components formed via electrolyte decomposition. The O 1s spectra exhibit analogous changes, with the growth of $[C{-}O^-]_2Mg^{2+}$ species upon discharge and recovery of the C═O signature upon charge. Meanwhile, the Mg 2s peak shifts to lower binding energies and increases in intensity during discharge, which reverts upon charge as well. The EDS mapping (Figure S24) confirms reversible variations in the cathode composition aligned with the electrochemical redox process, without signs of irreversible elemental loss or decomposition. Collectively, these results, as summarized schematically in Figure 5d, demonstrate that Mg^{2+} storage in NUPI occurs via a reversible, heterogeneous enolization mechanism (C═O ⇌ C─O^-/$[C{-}O^-]_2Mg^{2+}$) in the $Mg[B(hfip)_4]_2$/DME electrolyte system, consistent with the observed high specific capacity and improved charge-transfer kinetics. In contrast, cells using the $Mg(HMDS)_2$-based electrolyte display unstable spectral features and perturbed redox behavior, indicative of complex speciation and side reactions (Figure S25). Overall, a highly conjugated and well-ordered π–π stacked framework promotes intrachain electron delocalization and facilitates efficient charge redistribution during redox cycling, thereby stabilizing the radical intermediates generated during Mg^{2+} insertion and extraction. Simultaneously, strong π–π stacking and backbone planarity enhance interchain electronic coupling, increasing intrinsic electronic conductivity and minimizing localized electron accumulation at the cathode–electrolyte interface. This charge delocalization suppresses the formation of reactive surface sites that might otherwise trigger electrolyte decomposition. Furthermore, the weakly anion coordinating, chloride-free electrolyte imposes minimal perturbation on the polymer backbone, helping preserve

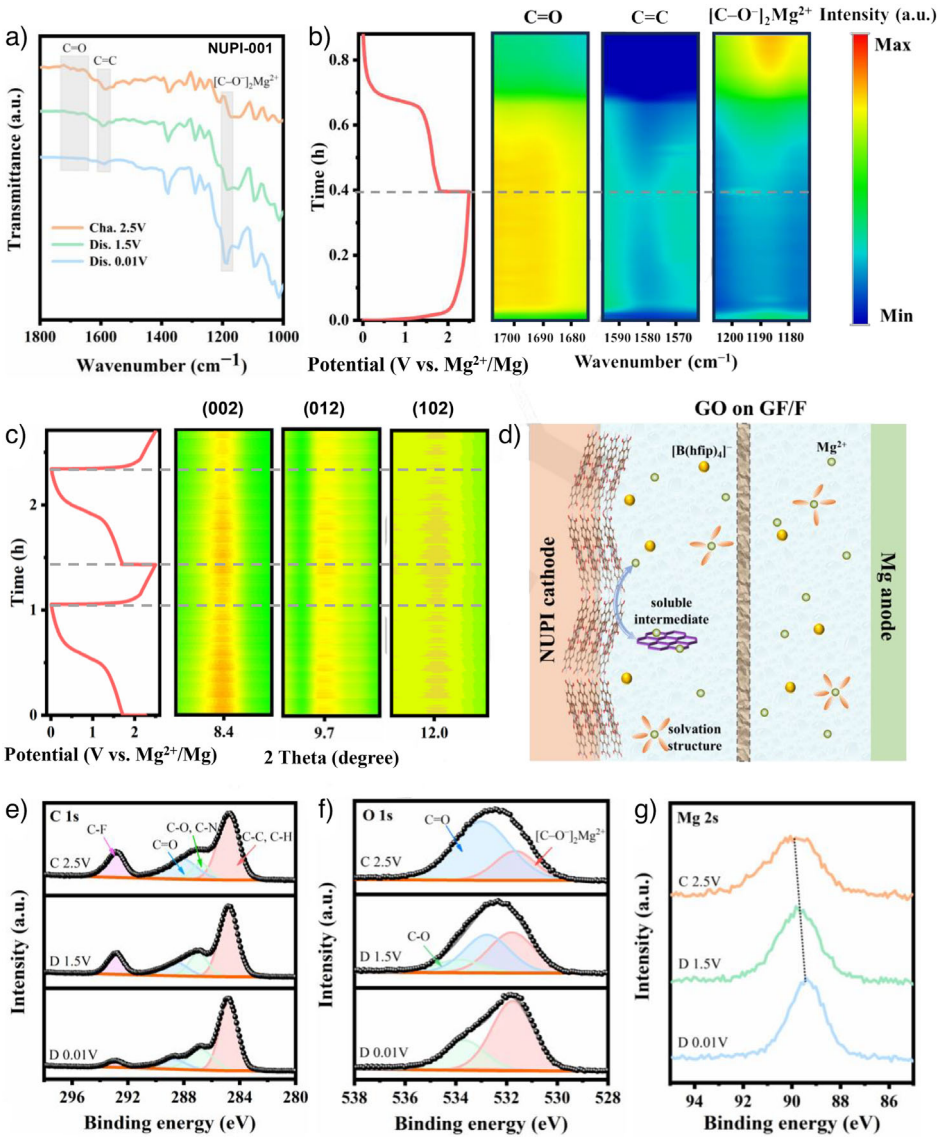

Figure 5. Redox chemistry of NUPI in $Mg[B(hfip)_4]_2$ over 0.01–2.5 V (vs. Mg^{2+}/Mg). a) Ex situ FTIR spectra at defined states of the 5th cycle. b) In situ synchrotron FTIR (SR-FTIR) contour map during galvanostatic cycling. c) In situ synchrotron XRD (SR-XRD) contour map. d) Schematic of the Mg-storage (enolization) mechanism. e)–g) Ex situ high-resolution XPS spectra: (e) C 1s, (f) O 1s, and (g) Mg 2s.

the ordered π–π stacking and extended conjugation. This structural preservation maintains a stable electronic network, enabling uniform charge distribution and reversible redox activity even under deep discharge and high cutoff voltage conditions. Thus, by coupling these synergistic molecular and electrolyte effects, the system achieves interfacial stability and reversible high-voltage cycling.

To elucidate the enolization chemistry and structural evolution of π-conjugated carbonyl PIs in MMBs, we performed DFT calculations on three-repeat-unit fragments of NUPI and PUPI (NUPI-3, PUPI-3) with dangling bonds saturated by hydrogen atoms. The ESP maps of NUPI-3 and PUPI-3 (Figure 6a) closely resemble those of the single-unit PIs (Figure 1a), with the most negative potential localized on the carbonyl oxygen atoms of both the urea diamine and dianhydride units, identifying these sites as the primary and most reactive Mg-coordination loci.[31] Projected density of states (PDOS) analysis (Figure 6b,c) shows N and O states in NUPI shifted to lower (more negative) energies relative to PUPI, indicating stronger electron withdrawal from the N–C=O moieties and enhanced orbital overlap within the C=O bonds—features that correlate with greater active-site durability during cycling.[32] Additional calculations that differentiate conjugated-backbone carbonyls from non-conjugated urea carbonyls reveal optimized magnesiation pathways in which Mg^{2+} preferentially bridges two adjacent conjugated carbonyls on the backbone (Figure 6d,e). The stepwise binding energies along this pathway are lower than for alternative configurations where Mg^{2+} bridges one conjugated and one urea carbonyl (Figure S26), implying that urea carbonyls are largely electrochemically inactive but beneficial for rotational flexibility and coordination stabilization.[33,34] Absolute ΔE values are not directly comparable across

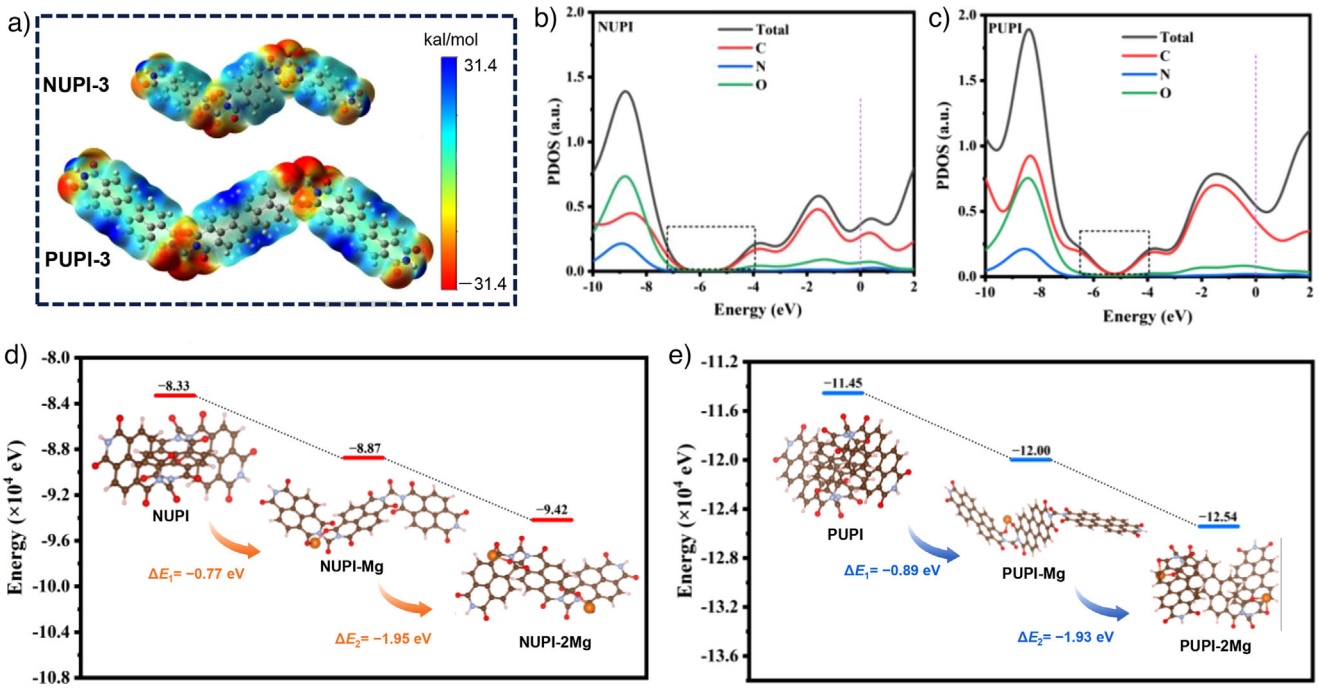

Figure 6. DFT analysis of NUPI and PUPI. a) Electrostatic-potential (ESP) maps of three-repeat-unit fragments (H-terminated). b) and c) Projected density of states (PDOS) for NUPI and PUPI. d) and e) Optimized magnesiation pathways, highlighting Mg^{2+} coordination to adjacent carbonyls in NUPI and PUPI.

the two polymers due to model simplifications and differences in the density/accessibility of conjugated active sites (e.g., NUPI's multilayer morphology affords more accessible sites).[18] Overall, the dominant storage proceeds through an enolization process in which two Mg ions initially coordinate to conjugated C═O groups, consistent with the in situ/ex situ spectroscopies.

Conclusion

In summary, we establish a rational co-design paradigm between conjugated PI molecular frameworks and electrolyte chemistry to unlock high-performance magnesium storage. Through systematic comparison of two structurally related yet electronically distinct PIs, NUPI and PUPI, in both chloride-containing and chloride-free electrolytes, we demonstrate that the extent and reversibility of enolization-driven Mg^{2+} storage is jointly dictated by molecular architecture and electrolyte stability. Chloride-free $Mg[B(hfip)_4]_2$/DME electrolytes offer broader electrochemical stability windows and more benign interfacial chemistry, enabling deep, reversible enolization of redox-active carbonyl sites. In this context, the layered, π-stacked morphology of NUPI promotes efficient Mg^{2+} transport and structural integrity, delivering superior capacity retention and rate capability. Operando FTIR/XRD, ex situ XPS, and DFT calculations collectively reveal a reversible, heterogeneous enolization mechanism (C═O ⇌ C─O⁻/[C─O⁻]$_2$$Mg^{2+}$) as the dominant Mg-storage pathway in conjugated PI frameworks. Notably, an NUPI cathode paired with $Mg[B(hfip)_4]_2$/DME and a GO-modified separator achieves a high reversible capacity of ≈175 mAh g^{-1} and an ultralow capacity fade of ≈0.05% per cycle over 1000 cycles at 500 mA g^{-1}. Our study elucidates the critical coupling between redox-site topology and electrolyte speciation in enabling fast, stable Mg^{2+} storage in organic hosts. These insights establish a versatile material-electrolyte design framework for next-generation MMBs and may be extended to other multivalent-ion chemistries.

Acknowledgements

X.H. acknowledges the China Scholarship Council (CSC) for financial support. This work was supported by the National Natural Science Foundation of China (Grant No. 52171186) and funding from the Center of Hydrogen Science, Shanghai Jiao Tong University, as well as the European Research Council under the European Union's Horizon 2020 Research and Innovation Program (grant agreement no. 770870, MOOiRE – A. V.; no. 101089281, MULTIMETAL-BAT – A. P.), the Fonds de la Recherche Scientifique—FNRS Postdoctoral Fellowship (Grant No. 40010559), and the FWO and F. R. S.-FNRS under the Excellence of Science Program (EOS 40007515). This work was also supported by the User Experiment Assist System of the Shanghai Synchrotron Radiation Facility (SSRF). The authors thank the staff at Beamlines (BL01B1 and BL02U2) of the Shanghai Synchrotron Radiation Facility. The authors also thank Dr. Wenjie Yu from the BL01B1 beamline for operando synchrotron FTIR measurements. The authors appreciate the

support from the Instrumental Analysis Center at Shanghai Jiao Tong University.

Conflict of Interests

The authors declare no conflict of interest.

Data Availability Statement

The data that support the findings of this study are available from the corresponding author upon reasonable request.

Keywords: Carbonyl organics · Chloride-free electrolytes · Enolization redox reactions · Magnesium metal batteries · Π-conjugated polyimides

[1] X. Lin, P. Apostol, H. Xu, V. R. Bakuru, X. Guo, Z. Chen, D. Rambabu, S. Pal, D. Tie, Y. Zhang, X. Xie, S.-G. Kim, Y. Li, Z. Li, M. Du, S. Yan, X. Zhang, R. Yuan, M. Zheng, F. Gauthy, V. Finsy, J. Zou, J.-F. Gohy, Q. Dong, A. Vlad, *Adv. Mater.* **2024**, *36*, 2312908, https://doi.org/10.1002/adma.202312908.

[2] B. Esser, F. Dolhem, M. Becuwe, P. Poizot, A. Vlad, D. Brandell, *J. Power Sources* **2021**, *482*, 228814, https://doi.org/10.1016/j.jpowsour.2020.228814.

[3] R. Cheng, Y. Min, H. Li, C. Fu, *Nano Energy* **2023**, *115*, 108718, https://doi.org/10.1016/j.nanoen.2023.108718.

[4] Z. Guo, S. Zhao, T. Li, D. Su, S. Guo, G. Wang, *Adv. Energy Mater.* **2020**, *10*, 1903591, https://doi.org/10.1002/aenm.201903591.

[5] R. Cheng, X. He, K. Li, B. Ran, X. Zhang, Y. Qin, G. He, H. Li, C. Fu, *Adv. Mater.* **2024**, *36*, 2402184, https://doi.org/10.1002/adma.202402184.

[6] X. He, R. Cheng, X. Sun, H. Xu, Z. Li, F. Sun, Y. Zhan, J. Zou, R. M. Laine, *J. Magnesium Alloys* **2023**, *11*, 4359–4389, https://doi.org/10.1016/j.jma.2023.11.008.

[7] X. He, R. Cheng, X. Sun, F. Sun, Y. Fu, Y. Li, P. Li, Z. Li, H. Xu, R. M. Laine, J. Zou, *Adv. Funct. Mater.* **2025**, *35*, 2413893, https://doi.org/10.1002/adfm.202413893.

[8] A. Nimkar, G. Bergman, E. Ballas, N. Tubul, N. Levi, F. Malchik, I. Kukurayeve, M. S. Chae, D. Sharon, M. Levi, N. Shpigel, G. Wang, D. Aurbach, *Angew. Chem. Int. Ed.* **2023**, *62*, e202306904, https://doi.org/10.1002/anie.202306904.

[9] X. He, S. Wang, X. Wu, C. Shu, X. Fan, Z. Yu, W. Huang, *High Perform. Polym.* **2021**, *33*, 528–537, https://doi.org/10.1177/0954008320967052.

[10] M. Zhang, L. Wang, H. Xu, Y. Song, X. He, *Nano-Micro Lett.* **2023**, *15*, 135, https://doi.org/10.1007/s40820-023-01104-7.

[11] H. Zhang, L. Qiao, M. Armand, *Angew. Chem. Int. Ed.* **2022**, *61*, e202214054, https://doi.org/10.1002/anie.202214054.

[12] S. Hou, X. Ji, K. Gaskell, P.-f. Wang, L. Wang, J. Xu, R. Sun, O. Borodin, C. Wang, *Science* **2021**, *374*, 172–178, https://doi.org/10.1126/science.abg3954.

[13] Z. Zhang, Z. Cui, L. Qiao, J. Guan, H. Xu, X. Wang, P. Hu, H. Du, S. Li, X. Zhou, S. Dong, Z. Liu, G. Cui, L. Chen, *Adv. Energy Mater.* **2017**, *7*, 1602055, https://doi.org/10.1002/aenm.201602055.

[14] W. Han, M. Li, Y. Ma, J. Yang, *Electrochim. Acta* **2022**, *403*, 139550, https://doi.org/10.1016/j.electacta.2021.139550.

[15] Z. Zhang, X. Chen, H. Zhang, W. Liu, W. Zhu, Y. Zhu, *Adv. Mater.* **2020**, *32*, 1907746, https://doi.org/10.1002/adma.201907746.

[16] X. Gao, Y. Chen, C. Gu, J. Wen, X. Peng, J. Liu, Z. Zhang, Q. Zhang, Z. Liu, C. Wang, *J. Mater. Chem. A* **2020**, *8*, 19283–19289, https://doi.org/10.1039/D0TA06326F.

[17] H. Wu, Z. Ye, J. Zhu, S. Luo, L. Li, W. Yuan, *ACS Appl. Mater. Interfaces* **2022**, *14*, 49774–49784, https://doi.org/10.1021/acsami.2c14206.

[18] W. Chen, Y. Chen, J. Li, S. Zhang, D. Zhang, D. Li, S. Wang, F. Yu, Y. Chen, J. Zhang, *Energy Storage Mater.* **2024**, *68*, 103349, https://doi.org/10.1016/j.ensm.2024.103349.

[19] B. W. Schick, V. Vanoppen, M. Uhl, M. Kruck, S. Riedel, Z. Zhao-Karger, E. J. Berg, X.u Hou, T. Jacob, *Angew. Chem. Int. Ed.* **2024**, *63*, e202413058, https://doi.org/10.1002/anie.202413058.

[20] X. Song, J. Sun, W. Ren, L. Wang, B. Yang, H. Ning, P. Zhang, Z. Caixiang, Z. Tie, X. Zhang, Y. NuLi, Z. Jin, *Angew. Chem. Int. Ed.* **2025**, *64*, e202417450, https://doi.org/10.1002/anie.202417450.

[21] H. D. Yoo, Y. Liang, H. Dong, J. Lin, H. Wang, Y. Liu, L. Ma, T. Wu, Y. Li, Q. Ru, Y. Jing, Q. An, W. Zhou, J. Guo, J. Lu, S. T. Pantelides, X. Qian, Y. Yao, *Nat. Commun.* **2017**, *8*, 339, https://doi.org/10.1038/s41467-017-00431-9.

[22] D. Wang, X. Du, G. Chen, F. Song, J. Du, J. Zhao, Y. Ma, J. Wang, A. Du, Z. Cui, X. Zhou, G. Cui, *Angew. Chem. Int. Ed.* **2023**, *62*, e202217709.

[23] M. Li, Q. Wang, J. Wang, L. Huang, J. Chu, X. Gan, Z. Song, *Chem. Eng. J.* **2023**, *456*, 141114, https://doi.org/10.1016/j.cej.2022.141114.

[24] H. Dong, O. Tutusaus, Y. Liang, Y. Zhang, Z. Lebens-Higgins, W. Yang, R. Mohtadi, Y. Yao, *Nat. Energy* **2020**, *5*, 1043–1050, https://doi.org/10.1038/s41560-020-00734-0.

[25] X. Gan, H. Zhang, Z. Hu, M. Li, J. Wang, T. Cai, Z. Chen, H. Gong, Y. Wang, Z. Song, *Adv. Funct. Mater.* **2025**, *35*, 2504093, https://doi.org/10.1002/adfm.202504093.

[26] Y. Zhao, S. Chen, M. Zhou, M. Pan, Y. Sun, D. Zhang, S. Zhang, Y. Wang, M. Li, X. Zeng, J. Yang, J. Wang, Y. NuLi, *ACS Nano* **2024**, *18*, 22356–22368, https://doi.org/10.1021/acsnano.4c06653.

[27] Y. Zhao, M. Zhou, X. Zeng, J. Yang, J. Wang, Y. NuLi, *Adv. Funct. Mater.* **2025**, *35*, 2423533, https://doi.org/10.1002/adfm.202423533.

[28] H.-g. Wang, S. Yuan, D. Ma, X. Huang, F. Meng, X. Zhang, *Adv. Energy Mater.* **2014**, *4*, 1301651, https://doi.org/10.1002/aenm.201301651.

[29] W. Chen, Y. Chen, H. Li, S. Zhang, D. Li, F. Yu, Y. Chen, W. Yan, J. Zhang, *Energy Storage Mater.* **2024**, *73*, 103779, https://doi.org/10.1016/j.ensm.2024.103779.

[30] F. Simon, J. B. Mitchell, R. Wang, C. Zhan, D. Jiang, V. Presser, V. Augustyn, *Chem. Rev.* **2020**, *120*, 6738–6782.

[31] Y. Zhu, W. Jin, H. Gao, Y. Chen, T.-R. Wu, D.-Y. Wu, Y. Huang, D. Guo, Z. Chen, Q. Huang, J. Cao, J. Xu, *Chem. Eng. J.* **2023**, *462*, 142229, https://doi.org/10.1016/j.cej.2023.142229.

[32] B. Mortemard de Boisse, G. Liu, J. Ma, S.-i. Nishimura, S.-C. Chung, H. Kiuchi, Y. Harada, J. Kikkawa, Y. Kobayashi, M. Okubo, A. Yamada, *Nat. Commun.* **2016**, *7*, 11397, https://doi.org/10.1038/ncomms11397.

[33] A. F. Shestakov, O. V. Yarmolenko, A. A. Ignatova, A. V. Mumyatov, K. J. Stevenson, P. A. Troshin, *J. Mater. Chem. A* **2017**, *5*, 6532–6537, https://doi.org/10.1039/C6TA10520C.

[34] A. F. Shestakov, O. E. Romanyuk, A. V. Mumyatov, S. Y. Luchkin, A. A. Slesarenko, O. V. Yarmolenko, K. J. Stevenson, P. A. Troshin, *J. Electroanal. Chem.* **2019**, *836*, 143–148, https://doi.org/10.1016/j.jelechem.2019.01.063.

Manuscript received: October 09, 2025
Revised manuscript received: November 25, 2025
Manuscript accepted: November 25, 2025
Version of record online: ■■, ■■